Modelling reactive diffusion in clays with two-phase-informed pore networks

Qingrong Xiong[*,1,2], Andrey P Jivkov[1,2], Syed M Ahmad[2]

[1]Research Centre for Radwaste & Decommissioning and Modelling & Simulation Centre, The University of Manchester, UK.

[2]School of Mechanical, Aerospace and Civil Engineering, The University of Manchester, UK.

Abstract

Development of pore network models for reactive diffusion of various species in clays is presented. Networks are constructed using experimentally measured pore-space and solid-phase characteristics. This way incomplete experimental information for the topological (pore connectivity) and the geometrical (inter-pore distances) properties of a given pore system can be balanced by known solid-phase properties. Opalinus Clay (OPA) is selected to demonstrate the application and validate the proposed model. OPA is modelled as anisotropic porous medium, reflecting preferential orientation of meso-porosity along clay bedding direction. Bulk diffusivities of various species (*HTO*, Cl^- and I^-) are calculated to investigate the effects of pore structure, anion exclusion and adsorption. Adsorption is simulated by

*Corresponding author. E-mail: qingrong.xiong@manchester.ac.uk; Tel: +44(0)7442159958 (Q Xiong)

changing the pore space, which is more realistic compared to existing reactive transport models with assumed constant pore geometry. Anion exclusion effects are simulated by introducing diffuse double layer (DDL) in the model. Results agree well with experimentally measured diffusion coefficients for transport parallel and perpendicular to the bedding direction. The proposed model is applicable to a large class of geo-materials and suitable for linking to lattice models for deformation and damage.

Keywords: Opalinus Clay, pore network model, diffusion, anion exclusion, sorption

1. Introduction

A thorough understanding of the porous media mass transport is of prime importance in various science and engineering applications, e.g., in radioactive waste disposal (Yu and Neretnieks, 1997; Bourg *et al.*, 2003), in remediation of contaminated groundwater (Grathwohl, 1998), in tracer studies in oil recovery (Whitaker, 1967). The transport properties such as permeability and diffusivity vary with pore space changes due to various mechanical, chemical, physical and thermal processes. These processes can be simulated and analysed by developing appropriate physical and microstructure-informed models. Such models are required to be able to predict measurable transport properties at a macro-scale (considering

45 engineering and geological aspects of the formation) from measurable pore
46 space characteristics such as pore shapes, pore size distribution. Pore-scale
47 level approaches, such as Smoothed Particle Hydrodynamics (SPH) (Zhu
48 and Fox, 2001) and Lattice Boltzmann (LB) (Kang *et al.*, 2006), have been
49 used for computing single and multiphase flow directly on pore-space
50 images. These methods are capable of treating complicated geometries and
51 are very useful for understanding pore morphology effects on transport.
52 However, they are computationally expensive and the conclusions that can
53 be drawn are limited to the imaged pore systems, which are not necessarily
54 representative for a larger volumes of the material analysed. In order to
55 perform simulations on representative elementary volumes (REV) of porous
56 media, such direct methods would require substantial computational effort.
57 Furthermore, pore space information for some materials (such as Opalinus
58 Clay (OPA)) and transport behaviour in these materials is dominated by
59 meso-porosity (pores with diameters between 2nm and 50nm) and micro-
60 porosity (pores with diameters smaller than 2nm) (NAGRA, 2002; Keller *et*
61 *al.*, 2011). The existing imaging techniques do not have sufficient resolution
62 to obtain detailed 3D images of such materials, to which methods, such as
63 SPH and LB, can be applied.
64
65 On the other hand, pore network models (PNM) offer simplicity and
66 computational efficiency that make them very attractive for modelling

transport through larger pore structures, e.g. of the order of tens to hundreds of inter-pore distances. It should be noted that PNM are conceptually scale indifferent, i.e. they can be applied to any length-scale interval where the structure of the pore space has been experimentally observed and analysed. For example, if a particular experimental technique allows for characterising pore features of sizes between 0.1 nm and 50 nm, the corresponding PNM can be constructed to capture effects within this length interval. In addition they provide a suitable representation of mutable pore space structures. In pore network models, the pore space is approximated by a set of sites and a set of bonds connecting some of the sites (Meyers and Liapis, 1999; Dillard and Blunt, 2000). Pore network models have to reflect the basic properties of porous media, such as shape and size distribution of pores and throats, as well as the pore coordination spectrum, i.e. the percentages of pores coordinated by different number of throats (Gao *et al.*, 2012; Jivkov *et al.*, 2013). These basic properties can be obtained in structures with distinguishable pores and pore throats. However, in materials such as Opalinus Clay (OPA), the pore space is dominated by pores smaller than 50 nm (NAGRA, 2002; Keller *et al.*, 2011), and due to the limitation resolution of current techniques the pore connectivity data cannot be extracted (Jivkov and Xiong, 2014). Hence, for such cases with limited pore space structure information, a different approach is required to construct effective pore networks. Previous approaches to tackle such incomplete pore space

89 information, including predefined connectivity to calculate length scale
90 (Xiong *et al.*, 2014), and variable length scale to calculate connectivity
91 (Jivkov and Xiong, 2014; Xiong and Jivkov, 2015), suffer from lack of an
92 additional constraint. Notably, the length scale refers to the distance
93 between the centres of neighbouring lattice sites, which corresponds to the
94 average inter-pore distances in the porous medium. This can be overcome
95 by considering the solid-phase structure of the material, e.g. the shape and
96 size distribution of mineral grains. The solid phase characteristics are
97 incorporated in this work to improve the realism of the constructed pore
98 network model (PNM). The new method developed in the work can be
99 coupled directly to the existing lattice models of the solid-phase previously
100 developed for analysis of damage evolution via micro-cracking (Jivkov and
101 Yates, 2012; Zhang and Jivkov, 2014).
102
103 The first objective of the work is to develop a methodology of pore network
104 construction for materials with partially available experimental data. The
105 second objective is to develop the model to account for anion exclusion and
106 adsorption effects on the mass transport. The third objective is to validate
107 the method with experimental data, for which OPA is selected.

2. Methodology

2.1. Experimental data

Opalinus Clay displays anisotropic responses to deformation and transport due to preferred orientation (or texture) of clay minerals attained during sedimentation and compaction (Wenk *et al.*, 2008). Specifically, experiments indicated anisotropic diffusion of solute species with slow diffusion perpendicular and fast diffusion parallel to the bedding plane. The goal is to construct a regular PNM in line with available structural data and macroscopic observations.

The pore space used in this work is OPA with sandy facies, labelled BDR in Keller et al. (Keller *et al.*, 2011; Keller *et al.*, 2013a), in which a large number of pores are located predominantly within the fine-grained clay mineral matrix. These pores with sizes > 10 nm, called meso-pores, were elongated in the bedding plane, which was resolved by Focused Ion Beam nano-tomography (FIB-nt). The porosity of meso-pores was θ_{mes} = 0.018. Pores with sizes < 10nm, called hereafter micro-pores, occupied approximately 9.7 vol.% (obtained from N_2 adsorption analysis). The porosity of micro-pores is thus θ_{mic} = 0.097. Further, the meso-pores were largely isolated and did not provide a percolating network through the sample. These definitions of micro- and meso-pores are aligned with the

129 commonly used in physical chemistry and may differ from other fields of
130 study.
131
132 The above two measurements were combined into a single 'cumulative pore
133 volume fraction – pore radius' curve given in Fig 1(a) (Keller *et al.*, 2011;
134 Jivkov and Xiong, 2014). For model construction the experimental
135 distribution of Fig. 1(a) is re-evaluated as cumulative probability separately
136 for meso- and micro-pores. These are shown in Fig. 1(b) and Fig. 1(c),
137 respectively.
138
139 Regarding the solid phase, Keller et al. (Keller *et al.*, 2013b) reported 18
140 vol.% non-porous carbonates with grain sizes ranging between 100 nm and
141 300 nm and 17 vol.% of non-porous quartz, the grain size distribution of
142 which was undetermined. For constructing the model for this study, the
143 reported data were converted into cumulative probability of carbonate grain
144 sizes as shown in Fig. 1(d). As both carbonates and quartz are non-porous,
145 the quartz is assumed to follow the size distribution of the carbonate
146 particles due to lack of quartz-specific experimental data.
147

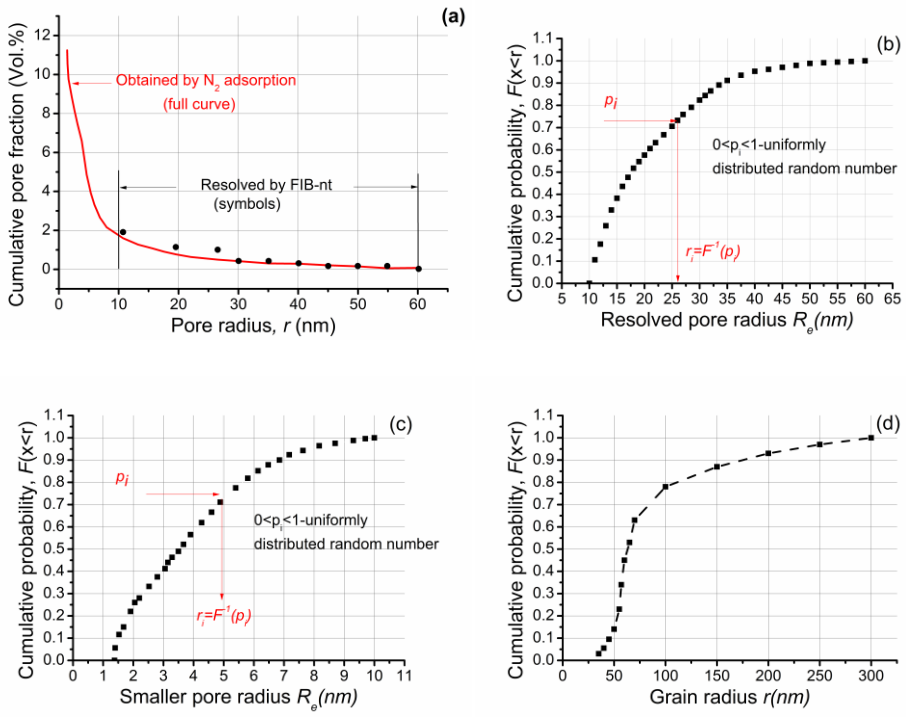

Fig. 1 Microstructure characteristics of Opalinus Clay: (a) cumulative pore volume fraction versus pore size determined by FIB-nt and N_2 adsorption analyses of sample BDR (Keller *et al.*, 2011); (b) cumulative distribution of meso-pore sizes; (c) cumulative distribution of micro-pore sizes with assumed probability density (Jivkov and Xiong, 2014); (d) cumulative distribution of carbonate grain sizes (Keller *et al.*, 2013b).

2.2. Pore network construction

Many pore networks are constructed based on different length scales due to the broad range of pore size distribution. A short overview of existing multi-scale pore network models is presented here.

Jiang et al. (Jiang *et al.*, 2013) developed a methodology to integrate networks extracted from images at distinct length scales. The pore network model was generated at each scale and then was integrated into a single two-scale network by characterizing the cross-scale connection structure between the two networks. The shortcoming of this method is that it is computationally costly due to the number of network elements (Bultreys *et al.*, 2015). Recognizing the computational problems when single micro-pores are taken into account, Mehmani and Prodanović (Mehmani and Prodanović, 2014) proposed a two-scale pore network by packing algorithms. The macro-network is constructed by Delaunay tessellation of the grain centres. Micro-porous networks are generated by downscaling existing networks extracted from macro-pores. This approach was capable of investigating fundamental two-phase flow properties of multi-scale porous media. A clear difference was observed between the behaviour of systems where micro-porosity was able to act in series with the macro-pores (intergranular or pore-filling micro-porosity) and systems where macro-porosity was able to act in parallel the meso-pores (intra-granular or dissolution micro-porosity). However, in the construction process, distorted pores were produced when many small grains touched a large grain. In addition, the ratio between macro and micro length scales needs to be determined for micro-porous regions. This ratio is difficult to obtain from image analysis, specifically for clays. Bultreys et al. (Bultreys *et al.*, 2015)

developed a workflow to integrate networks of macro-pores and micro-porous regions extracted from micro-CT images. This methodology allowed micro-porosity to act both in parallel and in series with the macro-pore network. However, a representative network for the micro-porosity is necessary. In addition, the pore networks from Jiang et al. (Jiang *et al.*, 2013) and Bultreys et al. (Bultreys *et al.*, 2015) are based on experimental data from micro-CT images which did not take into account the micro-pores that cannot be resolved by micro-CT. As the truncated cone shape is used to connect two neighbouring macro-pores, the tortuosity of the connection and geometric details about the bulk of the micro-porous cluster are neglected, which can lead to erroneous local conductivities. In this work, regular networks are used to generate models based on meso-porosity and micro-porosity.

The workflow is as follows: Firstly, the cellular basis is selected for allocation of grains and pores, which results in complementary (dual) lattices for solid and pore systems. In this work, the material was subdivided into cells, in which the truncated octahedrons represented the neighbourhoods of particles in the OPA. The truncated octahedron was the unit cell of a regular space tessellation, proposed for site-bond modelling of solids (Jivkov and Yates, 2012), which was used successfully for mechanical analysis (Jivkov *et al.*, 2012; Zhang and Jivkov, 2014) as well as

206 in the previous works on transport problems (Jivkov *et al.*, 2013; Jivkov and
207 Xiong, 2014; Xiong *et al.*, 2014).
208
209 The particles or grains are associated with cell centres (interiors). This is
210 illustrated in Fig. 2(a) for cells with equal distances between the three pairs
211 of square faces, a setup used in previous works (Jivkov and Xiong, 2014;
212 Xiong *et al.*, 2014). The geometry of the cellular assembly is described by
213 three length parameters, S_1, S_2, and S_3, measuring the distances between the
214 square faces in directions (1, 0, 0), (0, 1, 0) and (0, 0, 1), respectively. In an
215 assembly of N_c cells, the particle radius, r_i from Fig. 1(d), is assigned in
216 each cell. The volume of all allocated particles is required to be equal to the
217 experimentally-measured particle volume fraction, ϕ. From this requirement
218 the volume of a cell assembly is calculated by:

219
$$V_c = \frac{1}{\phi N_c} \sum_{i=1}^{N_c} \frac{4\pi r_i^3}{3} \quad \left(= \frac{1}{2} S_1 S_2 S_3 \right) \tag{1}$$

220 where V_c is the volume of a cell. The calculation of the three length
221 parameters from Eq. (1) depends on the selection of their ratios used here to
222 represent texture (a non-textured medium would have $S_1 = S_2 = S_3$).
223
224 Considering the fact that the reported pore radii are derived with the
225 assumption of cylindrical pore shapes (Keller *et al.*, 2011), a new pore
226 network structure is proposed. Firstly, a skeleton is formed using sites at the

centres of cell faces and bonds between neighbouring faces. This is illustrated in Fig. 2(b) on a single cell with $S_1 = S_2 = S_3$. The bonds show the positions where elongated cylindrical pores are allowed to reside, i.e. they represent potential diffusion pathways. Since pores reside on bonds, the sites at face centres represent pore junctions – volume-less containers redirecting mass transport. Then the experimentally measured porosity is mapped to the proposed skeleton. The meso-pores are allocated along cell boundaries according to their size distribution, relative porosity and in preferred direction(s), while the micro-pores with radii selected from Fig. 1(c) are assigned to bonds not already occupied by the meso-pores. The process terminates when the total pore volume fraction attains the experimental porosity. An example of a pore network model assigning meso-pores and micro-pore sets is shown in Fig. 2(c) and Fig. 2(d). More details about meso- and micro-pore allocation can be found in Jivkov and Xiong (Jivkov and Xiong, 2014).

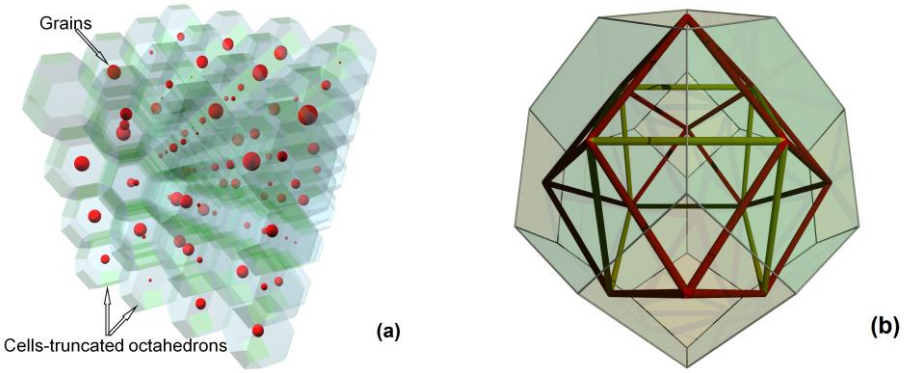

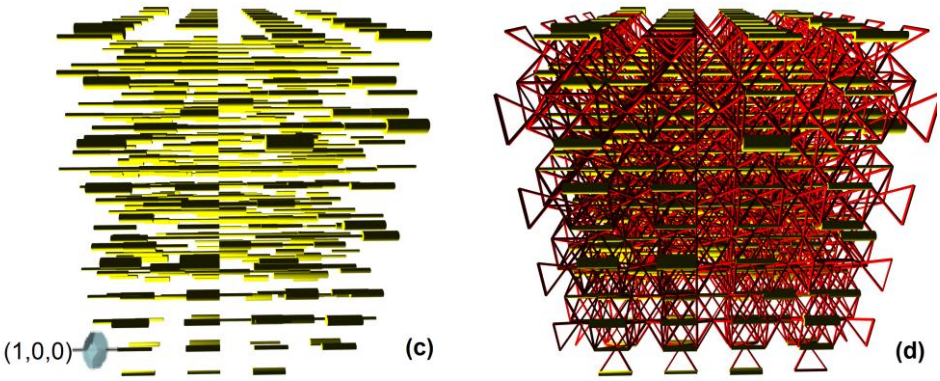

Fig. 2 (a) a cellular assembly, illustrating particles of variable sizes allocated to cell interiors; (b) unit cell illustrating potential diffusion paths (bonds) in the neighbourhood of central particle; (c) exclusive assignment of meso-pores along (1, 0, 0) taken as the clay bedding direction; (d) pore network model after assignment of meso-pores (yellow) and micro-pores (red). Examples are given on lattice with equal length parameters for bedding and out-of-bedding directions.

2.3. Pore diffusivities

Real pores and throats have complex and highly irregular geometrical profiles. In this work, a dimensionless circularity G was introduced to approximate pores as cylindrical capillaries with a constant cross section:

$$G = \frac{4\pi A_e}{P^2} \tag{2}$$

where $A_e = \pi R_e^2$ [nm^2] is the cross-section area, R_e = radius [nm] and P = perimeter [nm]. The overall pore shape in the clay matrix parallel and

perpendicular to the bedding is elongated with a mean circularity of 0.45 (Houben *et al.*, 2013).

The diffusion in the constructed model is driven by the concentration gradient along the cylindrical pores. For a pore with radius R_e, connecting nodes *n* and *m*, the mass flux of diffusing species, J_e [kg/m^{2}s], is described by Fick's first law:

$$J_e = -D_p \, G \Delta C_{nm} / L_e \tag{3}$$

where D_p [m^2/s] is the pore diffusivity, L_e [m] is the pore length, and $\Delta C_{nm} = C_n - C_m$ [kg/m^3] is the concentration difference between the ends of a throat. It is noted that in the pore bodies of this model are the cylindrically shaped network bonds, while the network nodes are only pore junctions, where concentrations are the main unknowns. Hence the gradient along the pore bodies is defined by the difference between the concentrations of the connected nodes.

The pore diffusivity of species of radius r_0 is defined by taking into account the steric hindrance effects (Bryntesson, 2002):

$$D_p = D_0 (1 - r_0 / \mathrm{R_e})^4 \tag{4}$$

where D_0 is the free molecular diffusion coefficient of the species in the medium filling the pore system. For a spherical molecule in a circular cylinder, the term, $(1-r^0/R_e)^4$, is a geometric hindrance factor based on the

molecule size and pore size and shape (Bryntesson, 2002). Pore diffusivities enter a graph-theoretical representation of PNM, allowing for efficient solution of the transport through the network via discrete analysis on graphs as detailed by Jivkov and Xiong (Jivkov and Xiong, 2014). The mass flow though a pore, W, is then $W = J_e \times A_e$.

2.4. Anion exclusion effects

The effective diffusion coefficients, which are a function of the tortuosity and constrictivity in the clay, and the accessible porosity, are different for various solutes (Appelo and Postma, 2005). In OPA, diffusion of anions is reduced relative to a neutral tracer such as tritiated water (HTO). The decreased diffusion is explained by anion exclusion effects. The anion exclusion effects are caused by the diffuse double layer (DDL) that surrounds the negatively charged clay surface. To calculate effective diffusion coefficients for anions, e.g. Cl^- and Br^-, the amount of DDL needs to be modelled firstly. According to Appelo and Wersin (2007), iodide cannot access half of the available porosity due to anion exclusion effect. Hence the amount of DDL-water is approximately equal to half of the porosity and the volume of DDL is achieved by increasing the layer thickness of DDL, r_t, in each pore. If $R_e < r_t$, the anions cannot pass through this pore, otherwise, the anion-accessible pore radius will be $R^* = (R_e - r_t)$.

In this work, the diffusion of HTO is firstly simulated with the total porosity, and then, model the Cl^- to find the anion-accessible porosity. The difference gives the amount of DDL-water which is assigned to be devoid of porosity. Iodide has the same accessible porosity as Cl^-. However, the flux front for I^- is retarded compared with that of Cl^- and Br^-. A likely explanation of this retardation is the linear adsorption of I^- onto the clay surface (Appelo *et al.*, 2010; Altmann *et al.*, 2012).

2.5. Adsorption effects

OPA has large specific surface area (Altmann *et al.*, 2012), high ion-exchange capacity (Altmann *et al.*, 2012), and adsorption affinity for ions, suggesting that long-term diffusivity of such species can be significantly affected by adsorption (Aytas *et al.*, 2009). The amount of species sorbed onto the solid, β, is described by the adsorption isotherm, $\beta = \beta\ (C_M)$, where C_M is the local concentration of species M in the solution. Different species have linear or nonlinear adsorption processes (MontTerriProject, 2010).

In order to simulate adsorption effect, the adsorption of species needs to be judged firstly. In this work, the species are assumed to be strongly adsorbed so that the estimate of the adsorption obstruction effect can be obtained by considering the adsorbate to be uniformly smeared into a layer of thickness, *t*, as described in Xiong et al. (Meyers and Liapis, 1999; Xiong *et al.*, 2014):

$$t^2 - 2tR_e + 8\theta R_e r_M / 3 = 0 \quad (5)$$

where r_M is the radius of the diffusing species. If $t < r_M$, the species should be weakly adsorbed. This means that the above adsorption equation (Eq. 5) underestimates the adsorption obstruction effect (Xiong *et al.*, 2014). In this case, the adsorption effects can be achieved by reducing the radii of throats by a layer of thickness r_M (Meyers and Liapis, 1999). The radius of a throat after adsorption becomes $R^* = R_e - r_M$. The distribution coefficient K_d of I^- is 0.02 cm^3/g, thus the linear adsorption isotherm, β, equals $K_d C_M$ (Van Loon *et al.*, 2003).

3. Results and discussion

With respect to a coordinate system (X_1, X_2, X_3) normal to the square faces of the unit cell (see Fig. 2b), a pore network skeleton within the boxed region ($0 \le X_1 \le 20S_1$, $0 \le X_2 \le 20S_2$, $0 \le X_3 \le 20S_3$) was used. Tests with increasing models sizes were initially performed. When the model size was $20S_1 \times 20S_2 \times 20S_3$, the variation of calculated diffusivity with different model realisations (grain size distribution and pore size distribution) reduced to under 10%, which was accepted as reasonable accuracy.

The selection of the two boundaries depends on the macroscopic diffusivity being analysed. Specifically, the boundary conditions used to calculate the macroscopic diffusivity D_1 parallel to bedding direction (1, 0, 0) are:; zero flux through all nodes on planes $X_2 = 0$, $X_2 = 20S_2$, $X_3 = 0$, $X_3 = 20S_3$. For calculating the macroscopic diffusivity D_2 perpendicular to the bedding direction, say (0, 1, 0), the boundary conditions are: prescribed

concentration C_0 in all nodes on plane $X_2 = 0$; prescribed concentration C_1 in all nodes on plane $X_2 = 20S_2$; zero flux through all nodes on planes $X_1 = 0$, $X_1 = 20S_1$, $X_3 = 0$, $X_3 = 20S_3$. An illustration is given in Fig. 3.

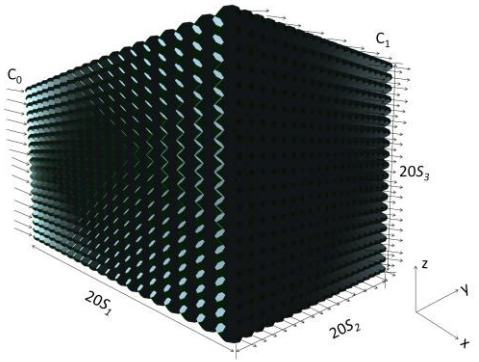

Fig. 3. Example of a pore network model (S_1=$2S_2$=$2S_3$) with applied boundary conditions: prescribed concentration C_0 in all nodes on plane $X_1 = 0$; prescribed concentration C_1 in all nodes on plane $X_1 = 20S_1$.

3.1. Texture effect on diffusivity

The pore networks constructed exhibit macroscopic tortuosity (path lengthening), introduced by the selection of diffusion pathways along the interfaces between solid-phase regions. This tortuosity depends on the material texture, represented here by the ratios of the cell length parameters in three perpendicular directions. Experimental results show that tortuosity is larger in a direction perpendicular to the bedding plane (Van Loon *et al.*, 2004). Therefore, the effects of larger cell length along the bedding plane and smaller cell lengths perpendicular to the bedding plane are investigated.

The out-of-bedding directions are not differentiated, i.e. the case of having $S_2 = S_3$ is assumed. The ratio S_1 / S_2 cannot be calculated directly from the currently available experimental information on the clay pore space. Since a lot of experimental data of HTO species diffusion has been published, we compare HTO experimental diffusivity to model predictions with variable S_1 / S_2 to find the ratio yielding best agreement. Once S_1 / S_2 is decided, the model can be used to simulate transport of other species such as neutral species and ions. Three ratios of the cell length parameters are considered: S_1 / S_2 = 2, 1.5, 1. For each cellular assembly of given ratio, 10 realisations of pore spatial distributions were analysed to obtain the diffusion coefficients along the bedding plane, D_1, and out-of-bedding directions, D_2. The results reported in Fig. 3 are the averaged values of these analyses on the basis of containing 35 vol.% solid particles. The calculated diffusion coefficients of HTO are in the following ranges: $D_1 = 3.09\times10^{-11}$~5.73×10^{-11} m^2/s; $D_2 = 1.42\times10^{-11} \sim 2.46\times10^{-11}$ m^2/s (see Fig. 3). Reported experimentally obtained values for HTO diffusion in OPA shown in Fig. 3 are $D_1 = (5.4\pm0.4)\times10^{-11}$ m^2/s (Van Loon *et al.*, 2004; MontTerriProject, 2010) and $D_2 = 1.13\times10^{-11} \sim 1.55\times10^{-11}$ m^2/s (Van Loon *et al.*, 2003; Joseph *et al.*, 2013). When $S_1/S_2 = 2$, the simulated results are closest to the experimental values. This ratio is used to calculate diffusivities for anions in the following section. The difference between the computational and the experimental results could be partially due to a

difference between the microstructure characteristics of OPA obtained by Keller et al. (Keller *et al.*, 2011; Keller *et al.*, 2013a) and used for model construction, and the clays used for experimental measurement of effective diffusion coefficients (Van Loon *et al.*, 2003; Joseph *et al.*, 2013).

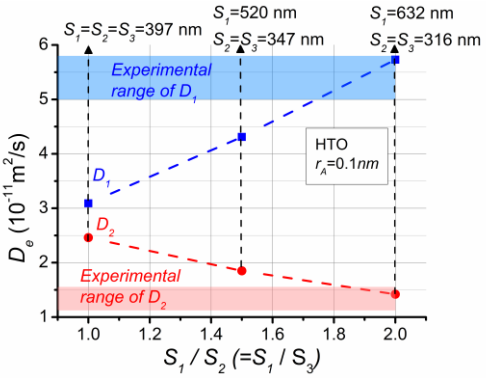

Fig. 4. Calculated macroscopic (effective) diffusivity of HTO in OPA. Clay textures are measured by the ratio of length parameters in the bedding, S_1, and the out-of-bedding, S_2, directions. D_1 and D_2 are the diffusion coefficients parallel and perpendicular to the bedding plane.

3.2. Anion exclusion and adsorption effect on diffusivity

The macroscopic diffusivities of Cl^- and I^- are shown in Table 1. The simulated results of Cl^- are very close to the experimental effective diffusivities (Van Loon *et al.*, 2003). The predicted D_1 of anions is a little overestimated and D_2 of anions is underestimated. This is in agreement with the expectations for the following reasons. Firstly, allocation of r_t leads to larger number of micro-pores belonging to DDL and a higher increase of

408 macroscopic tortuosity in out-of-bedding directions. Since pores allocated in
409 out-of-bedding directions are only micro-pores and the layer thickness of
410 DDL, r_t, assigned in each pore is the same. A larger fraction of micro-pores
411 is not accessible for the anions in out-of-bedding direction compared to the
412 number of pores in bedding plane direction. As a result, the effective
413 diffusivities in out-of-bedding directions are under estimated. Because the
414 total DDL volume is 50 vol.% of the pores and the micro-pores in out-of-
415 bedding directions contribute more to the DDL volume, the effective
416 diffusivities in the bedding plane direction will be over estimated. Secondly,
417 the accessible porosity for anions should be in a small range (Van Loon *et*
418 *al.*, 2003; MontTerriProject, 2010). This model can be used to calculate
419 other anion effective diffusivities which only have anion exclusion effects.
420
421 The diffusion behaviour of I^- is the effect of anion exclusion and adsorption.
422 Thus, the adsorption is simulated on the basis of the same accessible
423 porosity as of Cl^-. The predicted effective diffusivities of I^- are in agreement
424 with measured values as shown in Table 1. The over/under estimation of
425 experimental value, D_1 *and* D_2, is mainly due to the same reason (exclusion
426 effects) as for Cl^-. Another reason for difference between predicted results
427 and experimental values could be that the adsorption isotherm measured by
428 through-diffusion technique (Van Loon *et al.*, 2003) is not quite accurate to
429 describe adsorption onto pore walls.

Table1. Comparison of experimental (EXP) and computational (COM) results for diffusion of different species: D_0=free molecular diffusion coefficient; D_1= diffusivity in OPA bedding direction; D_2= diffusivity in OPA out-of-bedding direction. All diffusion coefficients are scaled by 10^{-12} m^2/s.

Species	D_0	D_1		D_2	
		EXP	MOD	EXP	MOD
Cl^-	2030	15~17	18	5.31~5.77	3.82
I^-	2000	10~14	16	4.28~4.86	3.36

Note: The free molecular diffusion coefficients D_0 at room temperature are obtained from Mont Terri Project (MontTerriProject, 2010). Experimental effective diffusivities are obtained from Van Loon, LR (Van Loon *et al.*, 2003).

4. Conclusions

This work presented:

- A new method for pore network construction, where solid-phase characteristics of a porous media are used to balance incomplete knowledge of geometrical and topological pore system characteristics;
- A framework for modelling the diffusion anion species due to purely anion exclusion effects in clay. This could be used to clarify the kinds of species transport (anion, cation or neutral species) in OPA,

as in most experiments, only species in the source reservoir solution are known. For example, if neutral species with comparable molecular size of HTO are assumed to diffuse in OPA, the accessible porosity applied to HTO could be used to simulate the diffusion of this species. If the simulated effective diffusivities are in good agreement with experimental values, the assumption is correct.

- An algorithm to simulate adsorption by changing pore space, which is more realistic compared to simulations based on constant pore geometry.

With simulations for three different solutes, it has been demonstrated that the outcomes are within the ranges of reported experimental data, particularly when clay heterogeneity is simulated via different length parameters along bedding plane and in directions perpendicular to the bedding plane. In principle, this model can also be applied to model other neutral species and anions.

The methodology is particularly suitable for modelling and simulation of micro- and meso-porous materials, such as bentonite and shale rocks. From one side, the existing experimental techniques do not allow for complete quantitative analysis of their pore systems. From another, the effect of

damage (micro-cracking) on mass transport in such materials is fundamental to the understanding of their retention or release functions.

As the description of the network topology is very important for accurately predicting residual phase saturation (Sok *et al.*, 2002), the feasibility of simulating multi-phase flow by the proposed PNM needs further study.

Acknowledgements

Xiong acknowledges gratefully the Doctoral Award from the President of The University of Manchester. Jivkov acknowledges the support from BNFL for the Research Centre for Radwaste & Decommissioning and from EdF R&D for the Modelling & Simulation Centre.

References

Altmann, S., Tournassat, C., Goutelard, F., Parneix, J.-C., Gimmi, T. and Maes, N. (2012) Diffusion-driven transport in clayrock formations. *Applied Geochemistry*, **27**, 463-478.

Appelo, C.A.J. and Postma, D. (2005) *Geochemistry, groundwater and pollution*. CRC Press.

Appelo, C.A.J., Van Loon, L.R. and Wersin, P. (2010) Multicomponent diffusion of a suite of tracers (hto, cl, br, i, na, sr, cs) in a single sample of opalinus clay. *Geochimica et Cosmochimica Acta*, **74**, 1201-1219.

Aytas, S., Yurtlu, M. and Donat, R. (2009) Adsorption characteristic of u(vi) ion onto thermally activated bentonite. *Jouranl of Hazardous Materials*, **172**, 667-674.

Bourg, I.C., Bourg, A.C.M. and Sposito, G. (2003) Modeling diffusion and adsorption in compacted bentonite: A critical review. *Journal of Contaminant Hydrology*, **61**, 293-302.

Bryntesson, L.M. (2002) Pore network modelling of the behaviour of a solute in chromatography media: Transient and steady-state diffusion properties. *Journal of Chromatography A*, **945**, 103-115.

Bultreys, T., Van Hoorebeke, L. and Cnudde, V. (2015) Multi-scale, micro-computed tomography-based pore network models to simulate drainage in heterogeneous rocks. *Advances in Water Resources*, **78**, 36-49.

Dillard, L.A. and Blunt, M.J. (2000) Development of a pore network simulation model to study nonaqueous phase liquid dissolution. *Water Resources Research*, **36**, 439-454.

Gao, S., Meegoda, J.N. and Hu, L. (2012) Two methods for pore network of porous media. *International Journal for Numerical and Analytical Methods in Geomechanics*, **36**, 1954-1970.

Grathwohl, P. (1998) Diffusion in natural porous media: Contaminant transport, sorption/desorption and dissolution kinetics (pod).

Houben, M.E., Desbois, G. and Urai, J.L. (2013) Pore morphology and distribution in the shaly facies of opalinus clay (mont terri, switzerland): Insights from representative 2d bib–sem investigations on mm to nm scale. *Applied Clay Science*, **71**, 82-97.

Jiang, Z., Dijke, M., Sorbie, K. and Couples, G. (2013) Representation of multiscale heterogeneity via multiscale pore networks. *Water Resources Research*, **49**, 5437-5449.

Jivkov, A.P., Gunther, M. and Travis, K.P. (2012) Site-bond modelling of porous quasi-brittle media. *Mineralogical Magazine*, **76**, 2969-2974.

Jivkov, A.P., Hollis, C., Etiese, F., McDonald, S.A. and Withers, P.J. (2013) A novel architecture for pore network modelling with applications to permeability of porous media. *Journal of Hydrology*, **486**, 246-258.

Jivkov, A.P. and Xiong, Q. (2014) A network model for diffusion in media with partially resolvable pore space characteristics. *Transport in porous media*, **105**, 83-104.

Jivkov, A.P. and Yates, J.R. (2012) Elastic behaviour of a regular lattice for meso-scale modelling of solids. *International Journal of Solids and Structures*, **49**, 3089-3099.

Joseph, C., Van Loon, L.R., Jakob, A., Steudtner, R., Schmeide, K., Sachs, S. and Bernhard, G. (2013) Diffusion of u(vi) in opalinus clay: Influence of temperature and humic acid. *Geochimica et Cosmochimica Acta*, **109**, 74-89.

Kang, Q., Lichtner, P.C. and Zhang, D. (2006) Lattice boltzmann pore-scale model for multicomponent reactive transport in porous media. *Journal of Geophysical Research: Solid Earth (1978–2012)*, **111**.

Keller, L.M., Holzer, L., Schuetz, P. and Gasser, P. (2013a) Pore space relevant for gas permeability in opalinus clay: Statistical analysis of homogeneity, percolation, and representative volume element. *Journal of Geophysical Research: Solid Earth*, **118**, 2799-2812.

Keller, L.M., Holzer, L., Wepf, R. and Gasser, P. (2011) 3d geometry and topology of pore pathways in opalinus clay: Implications for mass transport. *Applied Clay Science*, **52**, 85-95.

Keller, L.M., Schuetz, P., Erni, R., Rossell, M.D., Lucas, F., Gasser, P. and Holzer, L. (2013b) Characterization of multi-scale microstructural features in opalinus clay. *Microporous and Mesoporous Materials*, **170**, 83-94.

Mehmani, A. and Prodanović, M. (2014) The effect of microporosity on transport properties in porous media. *Advances in Water Resources*, **63**, 104-119.

Meyers, J. and Liapis, A. (1999) Network modeling of the convective flow and diffusion of molecules adsorbing in monoliths and in porous particles packed in a chromatographic column. *Journal of Chromatography A*, **852**, 3-23.

MontTerriProject. (2010) Long-term diffusion (di-a) experiment: Di-a2: Diffusion of hto, br^{-}, i^{-}, cs^{+}, $^{85}sr^{2+}$ and $^{60}co^{2+}$: Field activities, data and modelling. *Report TR*, 2009-2004.

NAGRA. (2002) Projekt opalinuston: Synthese der geowissenschaftlichen untersuchungsergebnisse *Technischer Bericht*, **02 -03**, 250-252.

Sok, R.M., Knackstedt, M.A., Sheppard, A.P., Pinczewski, W., Lindquist, W., Venkatarangan, A. and Paterson, L. (2002) Direct and stochastic generation of network models from tomographic images; effect of topology on residual saturations. *Transport in porous media*, **46**, 345-371.

Van Loon, L.R., Soler, J. and Bradbury, M. (2003) Diffusion of hto, $^{36}cl^{-}$ and $^{125}i^{-}$ in opalinus clay samples from mont terri: Effect of confining pressure. *Journal of Contaminant Hydrology*, **61**, 73-83.

Van Loon, L.R., Soler, J.M., Müller, W. and Bradbury, M.H. (2004) Anisotropic diffusion in layered argillaceous rocks: A case study with opalinus clay. *Environmental science & technology*, **38**, 5721-5728.

Wenk, H.R., Voltolini, M., Mazurek, M., Van Loon, L.R. and Vinsot, A. (2008) Preferred orientations and anisotropy in shales: Callovo-oxfordian shale (france) and opalinus clay (switzerland). *Clays and clay minerals*, **56**, 285-306.

Whitaker, S. (1967) Diffusion and dispersion in porous media. *AIChE Journal*, **13**, 420-427.

Xiong, Q. and Jivkov, A.P. (2015) Analysis of pore structure effects on diffusive transport in opalinus clay via pore network models. *Mineralogical Magazine*, **in press**.

Xiong, Q., Jivkov, A.P. and Yates, J.R. (2014) Discrete modelling of contaminant diffusion in porous media with sorption. *Microporous and Mesoporous Materials*, **185**, 51-60.

587 Yu, J.-W. and Neretnieks, I. (1997) *Diffusion and sorption properties of*
588 *radionuclides in compacted bentonite*. Svensk Kärnbränslehantering
589 AB/Swedish Nuclear Fuel and Waste Management Company.
590 Zhang, M. and Jivkov, A. (2014) Microstructure-informed modelling of
591 damage evolution in cement paste using a site-bond model.
592 *Construction and Building Materials*, **66**, 731-742.
593 Zhu, Y. and Fox, P.J. (2001) Smoothed particle hydrodynamics model for
594 diffusion through porous media. *Transport in porous media*, **43**,
595 441-471.
596